Digital Image Correlation

Michel Bornert, François Hild, Jean-José Orteu, Stéphane Roux

Digital Image Correlation

Michel BORNERT and François HILD and Jean-José ORTEU and Stéphane ROUX

6.1. Background

Digital Image Correlation or DIC, which appeared in the early 1980s [LUC 81, BUR 82, SUT 83, SUT 86] has a major impact in the field of the Mechanics of Solids and Structures. Nowadays, it is still undergoing very spectacular developments.

The challenge is to *measure* displacement *fields* of surfaces (or in volumes) of stressed specimens and structures from images acquired at different stages of loading. A specific advantage of this tool is that it exploits numerical images, which are usually acquired by optical means. Imaging devices have made significant progress not only in terms of quality and definition, but also (lower) cost. These imaging means are inherently contactless, non intrusive, tolerant to aggressive conditions (e.g., temperature, chemical environment), easy to use, efficient and cheap, many of these features that can only be appealing in the context of mechanical tests.

DIC can easily be used at different scales of space and time to the extent that it relies on principles applicable to pictures obtained by very different imaging systems. It is nowadays possible to use images shot by fast and ultra-fast cameras at time scales down to the microsecond or less [SCH 03a, SCH 03b, SIE 07, TIW 07, BES 08, BES 10], acquired by a scanning electron microscope (SEM) [DOU 00a,

DOU 00b, SOP 01, DOU 03, TAT 05, SUT 06, SUT 07a] or an atomic force microscope (AFM) [CHA 02, CHO 05b, CHO 07a, CHO 07b, HAN 10] at nanometric scales, but also satellite images at geophysical scales [SCA 92, LEP 07]. Multi-camera systems give access to 3D shapes and displacement fields of surfaces of an observed object (see Subsection 6.4). Three-dimensional images obtained by computed (micro)tomography [BAY 99, BOR 04, LEN 07, BAY 08, RAN 10] or magnetic resonance imaging [NEU 08, BEN 09] can also be utilized to measure 3D displacement fields in the bulk of various (optically opaque) materials.

The wealth of kinematic data obtained allows not only for a quantitative exploitation through identification techniques (see following chapters), but also to validate this identification, to enrich or degrade it according to the needs. By specifying appropriate forms of the displacement fields to be measured, image correlation can directly address this identification step (see Subsection 6.2.8).

6.2. Surface and Volume Digital Image Correlation

DIC techniques can be applied indifferently to classical two-dimensional or to volumetric images to which recent imaging tools give access. As a consequence, the term "pixel" will refer to in the following as the elementary discrete datum of a digital image defined in a two- or in a three-dimensional space. We detail in this section the algorithms providing evaluations of the apparent mechanical transformation Φ_a that links two images of the same mechanical system under two different configurations.

After a first subsection devoted to guiding principles and ingredients common to all presented algorithms, the discussion then will focus on so-called "local" image correlation techniques, which evaluate the transformation Φ_a piecewise, through a large number of independent analyses on sub-images, called "correlation windows" or "domains." Various flavors of the more recent "global" approaches, which may be enriched by some *a priori* mechanical information suited to each problem dealt with, will subsequently be described. The main sources of uncertainties and their quantification will be discussed in Section 6.3.

6.2.1. *Images*

The input data of the analysis are positive integers, called *gray levels*, of the image of the first configuration, known as the "reference image", noted f_I, and those of the second one, called the "deformed image", noted g_I, where the subscript I refers to a pair of integers (column, line) in the case of 2D images or to a triplet (column, line, plane) if 3D images are considered. These integers vary between 0 and some maximum value related to the *digitization* or *encoding depth* (or *dynamic range*) of the image sensor (e.g., 256 levels for 8-bit images, 4096 for 12-bit images). Indices I vary

in planar or volumetric domains, whose extension characterizes the *image definition* (e.g., $[0; 1023] \times [0; 1023]$ for a one-megapixel 2D image), and in which it is possible to define continuous positions, with real-valued coordinates $\boldsymbol{x}$ [1]. The two images can be extracted from a temporal sequence comprising a large number of images, of which any can be selected as the reference image or the deformed image. However we do not address in the following the algorithms that process such a sequence globally.

The images f_I and g_I result from a complex acquisition chain, today evermore various. It is essential to consider this acquisition process in the final interpretation of the estimated transformation, and to wonder about the presence of biases that could result from it. In particular, the analysis of this chain would make it possible to specify the link between some physical quantity continuously varying in space, denoted by $\tilde{f}$, and the discrete gray level f_I that this quantity induces through the imaging system at position I in the image. Because of space limitation, this aspect will not be developed herein.

DIC principles rest on the essential assumption that the physical quantity that leads to the image is associated with some physical property of the matter that constitutes the analyzed system, and, as a consequence, is transported by the sought apparent mechanical transformation Φ_a. Noting $\tilde{g}$ the continuous physical quantity associated with the deformed image, this assumption writes

$$\tilde{g}(\Phi_a(\boldsymbol{x})) = \tilde{f}(\boldsymbol{x}). \tag{6.1}$$

6.2.2. *Texture of images*

As will be made more specific later on, DIC exploits a texture that must be the signature of each surface (or volume) element, simply transported, according to Equation (6.1), by the displacement field, without any other deterioration. Moreover, the gray levels representing this texture in the images need to exhibit a broad dynamic range that covers as much as possible the available encoding depth of the images, i.e., from 8 to 16 bits, without however showing saturation. Lastly, it is desirable to have strong contrasts from one pixel to the next to be able to be sensitive to small displacement amplitudes.

The simplicity of the implementation of the method would recommend to rely on the natural texture of the studied material. This is sometimes possible, as illustrated in Figure 6.1. However, the correlation function of the texture will then dictate the performances of the analysis. Thus, for the example of the steel shown in the Figure 6.1a, the various phases revealed by a selective chemical etching have an orientation that will allow a good estimate of the displacement along the horizontal direction but a

1. In the following, $\boldsymbol{x}(I)$ is the point with integer coordinates I.

worse one in the perpendicular direction. In this context, the surface topography of silica observed by AFM (Figure 6.1c) does not lead to a strong sensitivity. Conversely, the phase image of the same zone (Figure 6.1d) can lead to a much better resolution. The selection of an appropriate mode of observation, associated, when required, with an adequate surface preparation, is thus an essential element for the use of natural contrast in DIC.

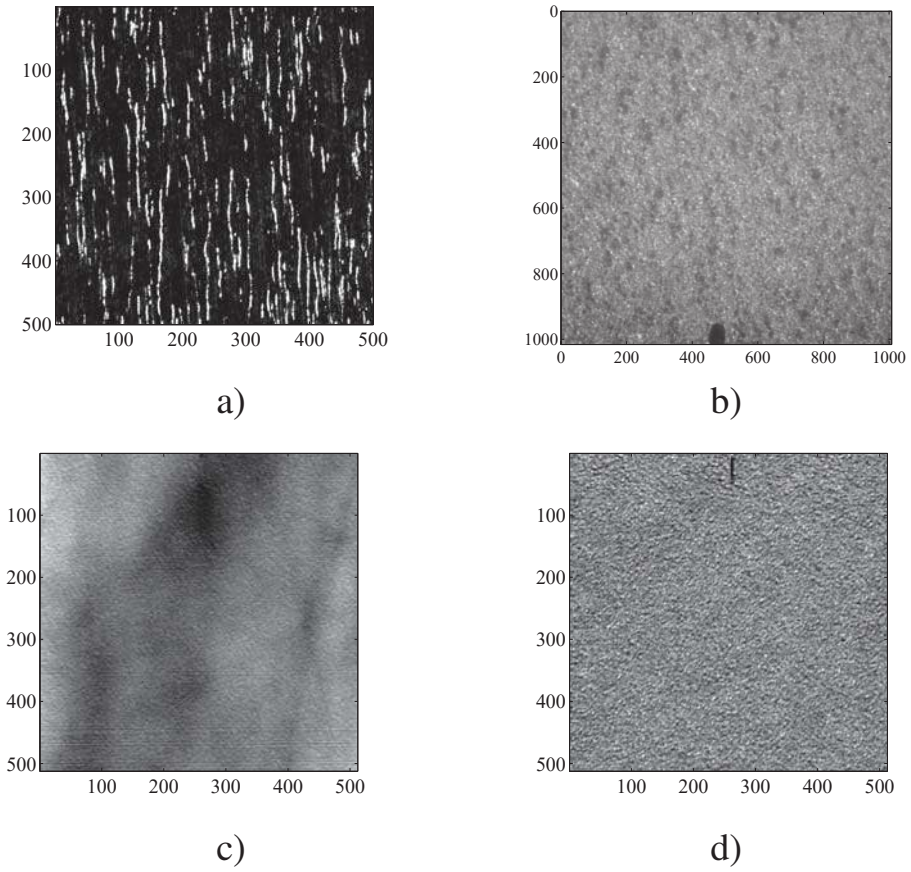

Figure 6.1. *Examples of natural image textures suitable for digital image correlation. a) 304L stainless steel (1 pix. = 3.2 μm); b) Silicon carbide (1 pix. = 1.85 μm); c) Topographic AFM image of a silica glass (1 pix. = 2 nm); d) Phase AFM image (same area as in c)*

The existence of such a contrast is not guaranteed. A possible way to circumvent this difficulty is to deposit an artificial texture on the surface of the studied samples as illustrated in Figure 6.2. The pulverization of fine droplets of black paint on a white background (or conversely) is a process called "speckle painting" that can be used on many materials. The airbrush allows to form an aerosol whose droplets size can be adjusted by an adapted nozzle. For the largest scales (for example for civil engineering structures) marking can be done with a stencil key set. A limitation can emerge from the strong deformability of materials as in the example of Figure 6.2c which is an elastomer. It is difficult for a painting to follow deformations of large amplitude. In

this case, a powder deposit (talc in this example) allows for a good stability of texture up to several hundreds percent of strain.

The deposition of particles on the surface can also be used in the context of scanning electron microscope (SEM) imaging [SCR 07]. Electron lithography techniques, in particular in their simplified version that can be implemented without expensive equipment other that the SEM itself [ALL 94], make it possible to mark surfaces by means of microgrids with a step varying from a few tens of micrometers to less than one micrometer, by metal deposition or chemical engraving. The periodicity of the obtained local contrast requires however some minor adaptations of the correlation algorithms to avoid offsets of one or several grip steps in the evaluation of the displacement field. An advantage if this type of marking is that it does not hide the microstructure and thus facilitates the micromechanical analyses of heterogeneous materials [DOU 00a, HER 07]. However the analysis cannot be as dense as with a fine speckle painting.

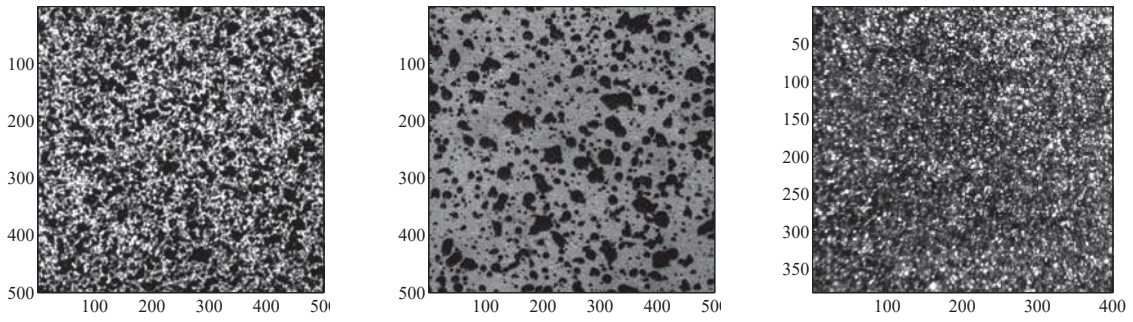

Figure 6.2. *Examples of artificial image textures suitable for digital image correlation*

Lastly, when three-dimensional images of computed tomography are to be exploited, a texture in the bulk of the studied material needs to be relied on (Figure 6.3). Some materials are then privileged, like most rocks [LEN 07], stonewool [HIL 09b], nodular graphite cast iron [RAN 10], or foams [ROU 08], whose micro-pores, inclusions or heterogeneous microstructure behave as a speckle painting. In the absence of such contrast or within the framework of an analysis at a finer scale, it is sometimes possible to reinforce it artificially (for example by diffusion of a heavy element to mark grain boundaries, or by addition of fine markers during the processing of the material [BOR 04]) but the difficulty is then to make sure that this marking does not introduce any modification of the mechanical properties, or to take into account the modified microstructure of the material in the interpretation of the results.

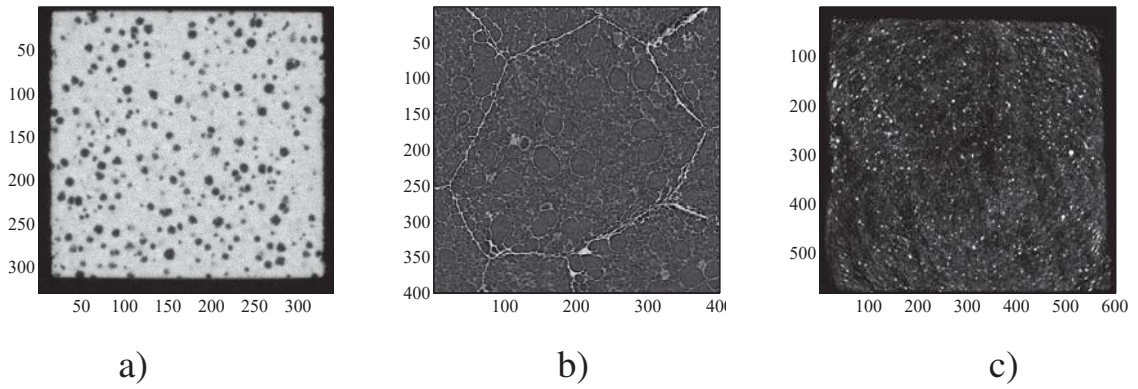

Figure 6.3. *Examples of sections through 3D X-rays computed tomography images; a) Cast iron with spheroidal graphite modules; b) Polymeric foam; c) Stonewool*

6.2.3. *Guiding principles*

The aim of the exposed methods is to evaluate the apparent transformation Φ_a on a Region Of Interest (ROI) R of the reference image starting from the knowledge of the gray levels f_I and g_I. This essentially is an *ill-posed* problem insofar as the available information (i.e., the gray levels of the pixels) is insufficient to uniquely determine a vectorial displacement at each pixel. It is thus imperative to regularize the problem by restricting this determination to a particular family of transformations $\Phi_0(\boldsymbol{\alpha}, \cdot)$, parameterized by N scalars, $\boldsymbol{\alpha}$, written here in vector form. Image correlation methods can then be given the following general formulation

$$\boldsymbol{\alpha}_{\min} = \underset{\boldsymbol{\alpha} \in V_\alpha}{\mathsf{Argmin}}\, C(\Phi_0(\boldsymbol{\alpha}, \cdot), R, [f], [g]) \tag{6.2}$$

where the *correlation coefficient* C is a scalar that measures the similarity [2] between the ROI R of the image $[f]$ (i.e., the set of the pixels f_I) transformed by $\Phi_0(\boldsymbol{\alpha}, \cdot)$ and the corresponding region of the image $[g]$. The parameters $\boldsymbol{\alpha}$ belong to a certain domain V_α of $\mathbb{R}^N$. The numerical resolution of this minimization problem leads to an evaluation $\Phi_0(\boldsymbol{\alpha}_{\min}, \cdot)$ of the sought transformation $\Phi_a(\cdot)$.

The various available image correlation algorithms derive from specific choices of the expressions of the correlation coefficient C (section 6.2.4), of the considered family of transformations and its parameter setting, which distinguish in particular the local methods (Section 6.2.6) from the global ones (Section 6.2.8), as well as of the minimization algorithms in use. Moreover, the evaluation of a continuous transformation from the knowledge of discrete values of gray levels provided by the input

2. By convention, one considers here that the similarity is larger when C is smaller, although the reverse could be adopted (by changing the sign of C for example).

images, requires to recourse to some interpolation method at some stage of the minimization problem. The various ways to do so define additional alternatives to specify image correlation algorithms (Section 6.2.5). These interpolation algorithms make it possible to evaluate the local displacement field with a resolution notably lower than one pixel, known as *subpixel* accuracy. For the sake of simplicity, the discrete nature of the input data will be ignored in the following presentation, except in Section 6.2.5 where this question is explicitly addressed. This simplification consists in assuming the pixels infinitely small with respect to the spatial gray level fluctuations, so that discrete gray levels f_I and g_I can be represented by continuous functions $f(\boldsymbol{x})$ and $g(\boldsymbol{x})$.

6.2.4. *Correlation coefficients*

The simplest and most classical similarity criterion is the sum of squared differences between the images [3]

$$C_1 = \int_R \left[f(\boldsymbol{x}) - g(\Phi_0(\boldsymbol{x}))\right]^2 \, \mathrm{d}\boldsymbol{x} = \int_R \left[f(\boldsymbol{x}) - g(\boldsymbol{x} + \boldsymbol{u}_0(\boldsymbol{x}))\right]^2 \, \mathrm{d}\boldsymbol{x} \qquad (6.3)$$

This quantity is clearly positive. It vanishes when the transformation Φ_0 coincides with the apparent transformation Φ_a and when the conservation condition (6.1) is exactly satisfied not only for the physical quantities $\tilde{f}$ and $\tilde{g}$ at the origin of the gray levels in the images, but also for the continuous gray levels f and g. The choice of a squared difference induces some operational advantages but may be replaced by an absolute value or any other measure of discrepancy.

Some imaging systems (e.g., SEM) do not make it possible to guarantee the stability of the conversion into gray levels f_I of the physical quantity $\tilde{f}$ at the origin of the image contrast and convected by motion according to Equation (6.1). One can then choose a less demanding similarity measure such as

$$C_2 = \min_{a,b} \int_R \left[f(\boldsymbol{x}) - (a\, g(\Phi_0(\boldsymbol{x})) + b)\right]^2 \, \mathrm{d}\boldsymbol{x} \qquad (6.4)$$

that consists in seeking the best linear regression between the gray levels of the two paired images. The optimized coefficients a and b can be interpreted as changes in contrast and brightness, respectively, of the image between the two configurations [4]. The optimization in Equation (6.4) is straightforward and leads to $a = \int_R (f - \bar{f})(g - \bar{g}) \, \mathrm{d}\boldsymbol{x} / \int_R (g - \bar{g})^2 \, \mathrm{d}\boldsymbol{x}$ and $b = \bar{f} - a\bar{g}$, where $\bar{f}$ and $\bar{g}$ are the averages of f and $g \circ \Phi_0$

3. For the sake of ease of notation, the various arguments of C are omitted in the following definitions.

4. If these changes can be quantified independently, it is possible not to carry out optimization, and to apply the criterion C_1 to the image f and the rescaled image $a\, g + b$.

over R. As $\int_R (f-\bar{f})^2 \, \mathrm{d}\boldsymbol{x}$ does not depend on Φ_0, optimizing C_2 is then equivalent to minimizing

$$C_3 = 1 - \frac{\left| \int_R (f-\bar{f}).(g-\bar{g}) \, \mathrm{d}\boldsymbol{x} \right|}{\sqrt{\int_R (g-\bar{g})^2 \, \mathrm{d}\boldsymbol{x} \int_R (f-\bar{f})^2 \, \mathrm{d}\boldsymbol{x}}} \tag{6.5}$$

which can be interpreted as the correlation coefficient of a linear regression and varies from 0 (perfect similarity) to 1 (no link between images) [5].

The definition of these criteria leads immediately to the definition of the image of residuals, whose gray levels defined on R are given by $f(\boldsymbol{x}) - g(\Phi_0(\boldsymbol{x}))$ or $f(\boldsymbol{x}) - (a\, g(\Phi_0(\boldsymbol{x})) + b)$, depending on which correlation criterion is considered. The qualitative or quantitative analysis of these residuals is a means of evaluating the relevance of the optimal transformation with respect to the actual unknown transformation. In case the registration would be perfect, and the residuals would contain nothing but image noise. It is worth noting that in this case and under the assumption of a moderate noise level, the criterion C_3 is equal at its optimum to $(1/2)(\sigma(f')/\sigma(f))^2$ where $\sigma(f)$ et $\sigma(f')$ are the standard deviations of the noiseless image f and of its noise f' on R. With an optimal contrast occupying the full dynamic range of the gray levels and a noise level of about 1% of the latter, as often observed with images of conventional optical cameras, the minimum of the C_3 coefficient might become as small as 10^{-3}. This concept of residuals will again be discussed in Section 6.2.8.

The above list of criteria is not exhaustive [CHA 11], but gathers those most commonly used for quantitative analyses in mechanics. Other similarity measures might be used within other image registration applications (e.g., satellite or medical imaging), in particular when the condition of convection of the gray levels is not well satisfied, because for instance of high noise levels [BOR 04] or of a too strong change of image contrast between the various configurations.

6.2.5. *Sub-pixel interpolation*

All DIC algorithms need to specify the interpolation method required to access a resolution in displacement notably less than one pixel. One should be aware of the fact that the associated technical choice might have strong consequences on the measurement accuracy.

The computation of the correlation coefficient, whatever the formulation kept among those presented in Section 6.2.4, needs to face the discrete nature of the images. The integration in equations (6.3)-(6.5) is in practice replaced by a summation over a

5. When suppressing the absolute value of the numerator of this expression, the criterion varies between 0 and 2, the maximum value corresponding to a "perfect inversion" of the contrast.

set of pixels in the reference image and requires to specify how the gray level in the deformed image at point $\Phi_0(\boldsymbol{x}(I))$ is calculated. This point has in general non integer coordinates and its gray level can only be evaluated by means of some interpolation scheme making use of the gray levels of surrounding pixels. There are numerous possible choices to do so, namely, evaluation by the gray level of the nearest neighbor, bilinear interpolation making use of the 4 first neighbors (8 neighbors for a trilinear interpolation in 3D), bi-cubic interpolation (various possible formulations) based on the 16 first neighbors (64 in 3D), spline functions to various orders, Fourier transforms on windows of adjustable size, or even wavelets. A high order interpolation will ensure the continuity of the correlation coefficient and of its derivative to various orders with respect to the kinematic parameters $\boldsymbol{\alpha}$, required by some optimization techniques, but will be greedier in computation time.

The errors induced by this interpolation takes the form of an over- or underestimation of the displacement components, which depends, on average, on its fractional part, expressed in pixels, as a consequence of the periodicity of the sensor behavior. The average of these errors is thus a function of this fractional part, which exhibits a symmetry with respect to the half-pixel displacement, and is often referred to as the "S-shaped" systematic error curve [CH0 97, SCH 00]. The precise shape and amplitude of this curve express the more or less good efficiency of the used interpolation scheme to restore the evolution of gray levels in an image induced by a real sub-pixel translation. This error needs to be quantified and, if possible controlled when small strains are to be analyzed, by means of the selection of an interpolation scheme adapted to the actual texture of the image, or conversely, by means of a modification of the latter [YAN 10], which depends on the marking of the sample but also on the parameters of the optical system.

Various procedures have been proposed to determine this S-shaped curve. One can for instance generate an artificial translated image from some real reference image and compare the results of the DIC analysis to the prescribed translation. However the representativity of the virtually translated image with respect to a real one itself depends of the used numerical translation procedure. A Fourier-based translation [SCH 00, HIL 06], consisting in a multiplication in Fourier space by a phase term, $e^{ik\delta}$, for each wave number k, is a particular procedure that leads to a C_∞ interpolation of the reference image, which exhibits some satisfactory properties with respect to this question. Another possibility is to numerically simulate the integration of the optical signal by the sensor [BOR 09, DUP 10] with now the difficulty to define a good numerical model of the sample texture. A last option consists in analyzing a pair or a sequence of real images corresponding to a well known transformation. This can be done but is delicate in practice for a pure translation [WAN 09], but can easily be achieved with out-of-plane motions that induce homogeneous apparent deformation gradients [YAN 10, DAU 11]. Recent analysis have also shown that this systematic error is strongly sensitive to image noise [WAN 09], at least for some algorithms [DUP 10].

It would ideally be advisable to reduce the amplitude of the systematic errors to a level less than that of the random errors, which correspond to the *fluctuations* of the measured displacements. The amplitude of the latter may also depend on the fractional part of the displacement field. When systematic errors are appropriately monitored, random errors constitute the actual limiting factor. This question will be addressed again in Section 6.3.2 to discuss measurement uncertainty.

6.2.6. *Local approaches*

In traditional approaches the transformation Φ_0 over R is decomposed into a multitude of *independent and local transformations*, or *shape-functions*, parameterized by the coefficients of their local expansion near centers $\boldsymbol{x}^0$ and used in the neighborhood D_{x^0} of these centers

$$\forall \boldsymbol{x} \in D_{x^0}, \quad \Phi_0(\alpha, \boldsymbol{x}) - \boldsymbol{x} = \boldsymbol{u}_0(\boldsymbol{x}) = \sum_i \Big[\alpha_i^0 + \sum_j \alpha_{ij}^1 (x_j - x_j^0) \\ \cdots + \sum_{jk} \alpha_{ijk}^2 (x_j - x_j^0)(x_k - x_k^0) + ...\Big] \boldsymbol{e}_i \tag{6.6}$$

where $\boldsymbol{e}_i$ is the unit vector along direction i in the image and x_i the coordinates of point $\boldsymbol{x}$ ($i \in \{1, 2\}$ in 2D and $i \in \{1, 2, 3\}$ in 3D). Zeroth-order methods are limited to the translation vector $\boldsymbol{\alpha}^0$ and were historically the first ones. First-order methods are the most common ones and take into account the components of the first deformation gradient $\alpha_i j^1$. There are thus six parameters to locally describe Φ_0 in 2D and twelve in 3D. Some variants include in addition the second order cross-terms (α_{112}^2 and α_{212}^2 in 2D, leading to a total of eight coefficients). One may also choose to restrict the local transformation to rigid motions (i.e., two translation components and one rotation angle in 2D, three components and three angles in 3D). Higher order expansions are seldom used.

With such a choice of local parametric description, the standard processing procedure consists in defining in the region of interest R a set of points $\boldsymbol{x}^k$, often organized into rows and columns (and planes in 3D) and usually regularly spaced, and to associate to each of them a small local domain D_{x^k}, in general square (or cubic in 3D), called *correlation window*, *subset* or *domain*. Problem (6.2) is then decomposed into as many independent optimizations leading to local parameters $\boldsymbol{\alpha}^k$ for each point $\boldsymbol{x}^k$, which define local estimations of the transformation Φ_a over the domain D_{x^k}, from which in general only the value $\Phi_0(\alpha^k, \boldsymbol{x}^k)$ at the center is retained. The final result is then a discrete collection of displacement vectors on a set of points $\boldsymbol{x}^k \in R$.

Such a description of the mechanical transformation by means of a set of local shape-functions requires thus essentially three choices, namely, the order of the local

transformation, the size of the correlation window and the sampling step of the ROI. These choices are usually left to the user in classical image correlation softwares, but they have some implications on the relevance of the kinematic measurements (displacement or strain). While questions relative to experimental errors will be addressed in detail in Section 6.3, the following aspects briefly are emphasized:

– the selection of the order of the local transformation is strongly linked with the window size. The systematic analysis performed in reference [BOR 09] on virtual images exhibiting non uniform deformation gradients with variable characteristic lengths demonstrates the existence of two error regimes. The first one is linked to the inaptitude of the shape function to describe the real transformation over the whole correlation window. This error is all the more important as the window is large, and that the order of the transformation is low. The second error regime, referred to as the *ultimate error*, coincides with the one encountered when the real transformation is a pure translation. It is on the contrary characterized by a decrease with window size and an increase with the order of the shape-function. This latter phenomenon is discussed in detail in Section 6.3.2;

– sampling step and window size can be chosen independently. One often selects a step less than or equal to the window size, so as to make use of the whole information contained in the image. An arbitrarily fine sampling of the image can even be chosen, at the price of an increased computation time. However one should be aware of the difference between this measurement step and the spatial resolution of the measurement of the displacement field, which remains controlled by the correlation window size. The displacement measurement associated with each position of the ROI sampling is the result of some averaging process over the whole correlation window;

– the sampling step may be a parameter entering implicitly or explicitly in the procedures used to compute strain components from the discrete values of the displacement components evaluated at each measurement point. We refer to Chapter 7 for a deeper discussion of this question. Note however that the accuracy of the measurement of the components of the deformation gradient relative to some gauge length is inversely proportional to the latter. When low strain levels are to be quantified, one should then privilege larger sampling steps or make use of differentiation procedures based on displacements evaluated over several sampling steps [ALL 94]. Moreover, in case of overlapping correlation windows, measurements of displacement at neighboring positions are no longer independent, which may induce some bias in the computation of the gradient components.

– the DIC analysis results in a discrete sampling of the displacement vectors (and their gradients) over a regular mesh of the ROI, the value at each sampling point being itself some average of the local displacement field over the correlation window. In order to define a displacement field at each position $\boldsymbol{x}$ in the ROI, these values need to be somehow interpolated. There is however no systematic way to evaluate the distance between the interpolated displacement field and the experimentally investigated field.

To conclude this short description of local formulations, let us note that they can also deal with an arbitrary selection of measurement points, adapted to the problem under consideration. These points may for instance be defined as the nodes of the finite element mesh of a structural calculation modeling the experiment [HER 07], as some isolated points of interest when the analysis does not require a dense evaluation of the kinematics — in such a case, the DIC techniques would operate as a markers tracking technique — or as the only points with an appropriate local image contrast, in case of a DIC analysis of a system with a non uniformly distributed natural local contrast. Local formulations can also make use of arbitrarily shaped correlation windows, for instance associated with some discrete entities of the considered system (such as the grains in a sand sample [HAL 10]), or delimited by characteristic boundaries of the system (such as for instance the interface between constitutive phases of a heterogeneous material [RUP 07]). The use of image masks is useful for the practical implementation of such alternatives of the general algorithm.

6.2.7. *Optimization algorithms*

At this stage, it is possible to compute C and its gradients for any set of parameters $\boldsymbol{\alpha}$. The optimisation, Equation (6.2), can then in principle be performed with any iterative numerical algorithm. A minimization algorithm making use of gradients (e.g., gradient descent, Newton-Raphson, Levenberg-Marquardt) or not (e.g., simplex, Powell) will allow to converge more or less quickly towards a local minimum close to the initializing set of parameters. In order to avoid convergence to an erroneous local minimum, various strategies might be employed, such as the preliminary systematic scanning of a set of displacement fields sufficiently large to contain the actual one, the use of known displacement fields relative to a previous stage of the mechanical test, or of the displacement of already analyzed neighboring positions, in the context of a "propagating front" type algorithm, or even, in the most difficult cases, the assistance of an operator. In this context, the preliminary systematic scanning is often restricted to integer components of the translation vector α_i^0, with other possible parameters set to zero or frozen to some other value determined by some other mean. To speed up this calculation stage, the gray level interpolation scheme may be set to a simple nearest neighbor algorithm; an alternative is to compute correlation coefficients in Fourier space, by means of efficient fast Fourier transform algorithms.

It is also possible to make use of these discrete evaluations of the correlation coefficient to interpolate this quantity by a bi-quadratic (or tri-quadratic in 3D) polynomial function near its discrete optimum, making use of the 9 (or 27) discrete values surrounding this optimum, and to analytically seek the continuous optimum of this interpolating function. Such an algorithm allows to reach a sub-pixel accuracy at a particularly low computation cost [WAT 01], but is restricted to the optimization of a limited number of components of the vector $\boldsymbol{\alpha}$.

Another proposed strategy to avoid local minima consists in a multi-scale algorithm [GAR 01a, HIL 02]. The idea is to start with strongly low-pass filtered images in order to artificially enlarge the well associated with the global minimum and to avoid local trappings far away from the solution. The obtained estimate is however not accurate as details of the image have been filtered out. The strategy consists then in gradually restoring these details and to perform the optimization again with these richer images, starting the algorithm with the displacement obtained on the coarser images, until the original image is recovered. This procedure (which also applies to the global approaches described in following section) turns out to be extremely robust and makes it possible to benefit from an optimization by descent, while limiting the effects of local minima.

This wide variety of options, which can be combined with each other, leads to a very vast range of DIC algorithms, which in addition will be enriched by the global approaches described in the following section. The selection of a particular combination of options is a compromise, whose definition depends on the available local image contrast, the awaited level of strain, the required measurement resolution and its spatial resolution, as well as on the numerical cost and the robustness of the algorithms.

6.2.8. *Global Approaches*

The main difference between local and global approaches is the choice of the displacement basis used to account for the transformation Φ_0 and its spatial definition. The local approach results in an independent calculation of the transformation on each correlation (small) window. However, no specific regularity of the displacement field is exploited. Conversely, it is possible to make the choice of a continuous transformation basis in a global approach. The displacement field is expressed as

$$\boldsymbol{u}_0(\boldsymbol{x}) = \Phi_0(\boldsymbol{\alpha}, \boldsymbol{x}) - \boldsymbol{x} = \sum_i \alpha_i \boldsymbol{\psi}_i(\boldsymbol{x}) \tag{6.7}$$

where the fields $\boldsymbol{\psi}_i$ form the chosen kinematic basis that can be defined over the whole region of interest. There is no restriction at this stage for the definition of this basis. The superposition of different displacement fields throughout domain R makes interdependent the sought amplitudes $\boldsymbol{\alpha}$, hence the term global to address this problem. The determination of $\boldsymbol{\alpha}$ is performed as above, namely, via the minimization of the sum of squared differences, $C_1(\Phi_0(\boldsymbol{\alpha}, \cdot), R, [f], [g])$. A Newton-Raphson scheme, which resorts to successive linearizations, is implemented to determine the solution, provided the amplitudes of the displacement fields are sufficiently small. As mentioned above, a multi-scale strategy can significantly relax this requirement [BES 06], and large displacements can be measured.

Unlike interpolated fields obtained with a local approach, each pixel is directly confronted with the value of the displacement field at this point and no interpolating

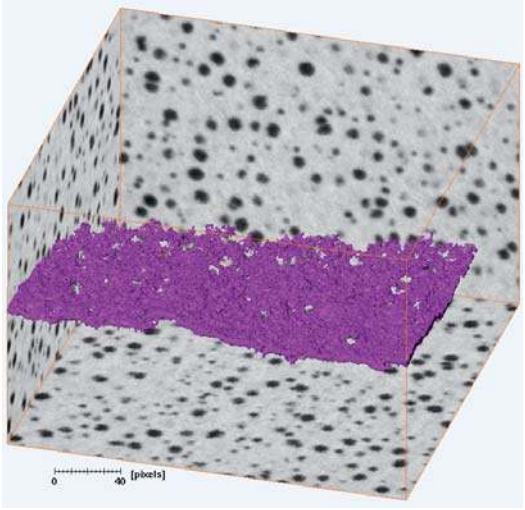

Figure 6.4. *Three-dimensional residue field showing the concentration of errors on the support of the crack (after [RAN 10])*

step is required. The correlation residual normalized by the dynamic range of gray levels is comparable to that encountered in local approaches, i.e., of the order of one percent. As mentioned in Section 6.2.4, the residual field allows the correlation errors to be spatially located. This property allows the user to quickly check for the good convergence of the algorithm, and especially to possibly correct / extend the chosen basis of fields. For example, if a fractured medium is observed and the chosen displacement basis is continuous, then the residual error will focus on the support of the kinematic discontinuity. This is a very effective way of precisely locating the crack front in all its geometric complexity [RAN 10] as shown in Figure 6.4.

The nature of the kinematic basis was not specified beyond its overall character. Great latitude exists for this choice. Sometimes some specific information (or assumptions) on the expected displacement field are available, and this is a valuable guide in the choice of this basis. Let us cite some examples:

– Without any specific information on the kinematics, the representation of the displacement field by shape functions of finite elements is a convenient possibility that will enable for an easy and direct interface with numerical simulations. So-called Q4-elements in two dimensions [BES 06], or C8-elements in three dimensions [ROU 08] (i.e., four-noded quadrilaterals with bilinear interpolation (2D) or 8-noded cubes (3D) with trilinear interpolations) are very well adapted to the discretization of the image. An example of a displacement field obtained with Q4 elements is shown in Figure 6.5(left). It is also possible to work with an unstructured mesh [LEC 09] or to use different shape functions [RET 09a]. Specific finite elements can then be considered with an enriched kinematics as in the extended finite element method (X-FEM) framework [RET 08] to add discontinuities in a given mesh (see Chapter 14). Last,

the fact that discretizations of the displacement field are shared with numerical modeling makes the coupling direct and *seamless* between image correlation on the one hand with e.g., an elastic calculation on the other hand (see [RET 09b] for such an example).

– The test can be analyzed with an analytical expression for the displacement field in the context of an elastic behavior. This solution can be an element of the selected kinematic basis. It is generally supplemented by additional degrees of freedom (such as rigid body motions). An example of this approach is the analysis of diametral compression (i.e., 'Brazilian test' [HIL 06]) or a point force loading (i.e., Flamant's problem [ROU 05]). Note however that the solution involves the Poisson's ratio ν of the material. If it is not known, the general solution can be split into two terms, one dependent on ν, and the other not. Similarly, the amplitude of the displacement field (except rigid body motions) is proportional to the ratio of the mechanical loading level to the shear modulus of the material. Thus by measuring the amplitudes of the basic fields, associated with the knowledge of the load level, allow to directly assess the elastic properties of considered medium [ROU 05]. Beyond the pure kinematic measurement, we begin to see the identification of mechanical properties (elastic in that case) without additional work via global digital image correlation.

– A particularly important case concerns cracks [ROU 06, ROU 09]. A family of analytical solutions exists, namely, Williams' series [WIL 57], which satisfies the cancelation of the tractions on the crack mouth. An appropriate selection of some terms of this infinite series can account for the sought displacement field in the vicinity of the crack tip. Among the selected fields, it is natural to include those associated with a $1/\sqrt{r}$ singularity for the stresses and strains. The amplitudes of these fields are related (via the physical size of the pixel and elastic properties of the medium) to the stress intensity factors in modes I and II. An example of such a determination is shown in Figure 6.5(right) for the same pair of images as that used in the left part of the figure. However, this family of fields requires *a priori* knowledge of the geometry of the crack (here assumed to be straight). The support of the crack is generally easy to appreciate as apparent in the displacement field or in the residual field (see Figure 6.4). The position of the crack tip is yet another issue. One solution is to use specific terms of Williams' series (i.e., strain and stress fields with $r^{-3/2}$ singularity [ROU 09]). The amplitudes of these fields provide information about the actual position of the crack tip.

– When considering slender objects, beam-type models are often used. This description assumes a particular (e.g., Euler- Bernoulli) kinematics that can be taken into account as in the displacement basis. This approach then allows to assess by image correlation the motion of a beam or a frame in a language directly suitable for modeling purposes [HIL 09a]. In this context, it is possible to finely characterize nonlinear modes (e.g., plastic hinge formation) in the framework of the strength of materials (i.e., constitutive law of a localized mode, equivalent position of a point corresponding to a localized failure mechanism, see Chapter 12). Moreover, the measurement

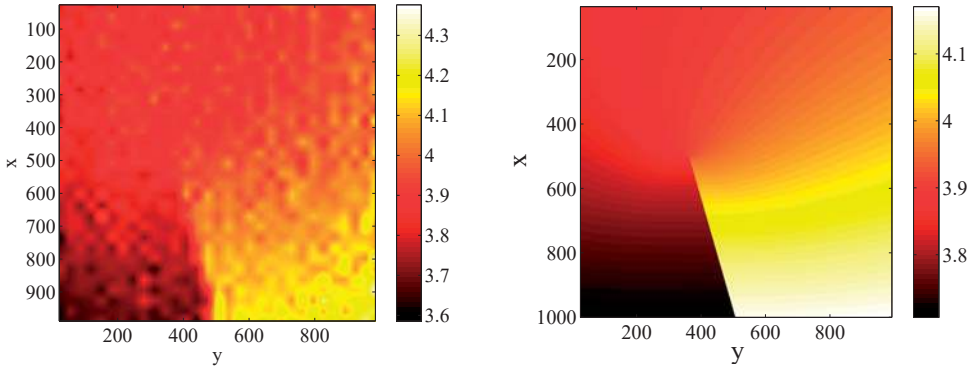

Figure 6.5. *Horizontal displacement component obtained on a silicon carbide specimen with (left) Q4 finite elements (of size 32 pixels) or an integrated approach with few closed-form solutions (right). The physical size of one pixel is* 1.85 μm*. The displacements are expressed in pixels (after [ROU 09])*

with an elastic kinematics over a given part of the beam gives access to the actual loading conditions.

– Beyond elasticity, it is sometimes possible to have *a priori* information to define a suitable displacement basis. The formation of shear bands in a uniaxial tensile test results in specific fields obeying Hadamard's conditions that can be accounted for (see Chapter 14).

– Last, the basis fields can be computed numerically. If one wishes to consider several unknowns (e.g., boundary conditions, material parameters) it suffices to calculate the various fields associated with changes in the parameters associated with the unknowns of the problem and consider them as a kinematics basis. The value of the amplitudes of these fields correspond to the best evaluation reflecting the observed situation [LEC 09].

6.3. Errors et uncertainties

Image correlation gives access to quantitative measurements of displacement fields. It is therefore crucial to assess the sources and levels of error and uncertainty associated with its implementation.

6.3.1. *Main Error Sources*

The first source of error is extrinsic to DIC because it results from image acquisition. Among them, let us cite:

– those related to the 3D-2D projection, which will be described in more details in Section 6.4. In particular the out-of-plane motions can induce artificial yet quantifiable displacements and strains [SUT 08b]. The use of telecentric lenses largely restricts some of these artifacts. It is also possible to correct for variations in optical magnification induced by global motions of an object with respect to the imaging system if one has an additional means for quantifying them [YAN 10].

– those related to the imperfect positioning of pixel coordinates. For optical images, the distortions induced by objective lenses fall within this category. For images obtained by scanning (e.g., SEM, AFM) the imperfect positioning of the locally probed area (by the electronic spot or cantilever tip) may also introduce significant spurious strains.

– those due to intrinsic noise in images. Two images acquired in identical conditions have gray levels that differ by a random amount whose standard deviation varies typically between a few thousandths (very good camera) and a few tenths (SEM image acquired very quickly) of the dynamic range of the gray levels. Its impact on image correlation [ROU 06] is detailed in Section 6.3.3.

A second category of errors is due to DIC:

– The selected basis of displacement fields is unable to describe the apparent transformation Φ_a. This error regime has already been mentioned in Section 6.2.5 and has been investigated in detail in Reference [BOR 09] for various softwares based on local approaches.

– The second type of error is related to the way the gray levels (or correlation coefficient) are interpolated in the correlation procedure when moving images for non-integer values (Section 6.2.5).

One could also mention the errors induced by possible changes of local contrast and brightness invalidating the basic assumption of gray level conservation (6.1). If their modeling is accessible, it is possible to take them into account [HIL 12b] in the correlation procedure (e.g., for the analysis of AFM images [HAN 10]). Last, when talking about errors or uncertainties, it is important to remember that the correlation residuals are very good indicators. They provide information on the local quality of the registration between images. They also allow for the modification or enrichment of the chosen kinematic basis [RET 08, RAN 10].

6.3.2. *Uncertainty and Spatial Resolution*

The choice of the discretization of the displacement field is crucial. Systematic studies on virtual images show two different regimes of error occur [BOR 09]. The first is related to the inability of the shape function to describe the actual transformation of the entire correlation window (for a local approach) or the discretized kinematics (for a finite-element based global approach). The second type of error, referred

to as ultimate, is similar to that encountered for pure translation transformations. It is characterized by a decrease of the error with the window size and increased order of the function shapes. It is a direct consequence of the ill-posedness of the correlation problem (6.2). The information contained in a small correlation window will only identify a limited number of parameters and the increase in their number will be accompanied by an increasing uncertainty of the value of each of them. The user is faced with a dilemma, which is comparable in some ways to Heisenberg's uncertainty principle, where position and displacement cannot be fully resolved simultaneously. Good spatial resolution (i.e., small window or element size) will be accompanied by a high displacement uncertainty and vice versa. A way of breaking this limit is to resort to regularized DIC [ROU 12] or Digital Volume Correlation [LEC 11].

To quantify *a priori* the measurement uncertainty, we restrict ourselves to the second case by choosing a simple kinematics (i.e., uniform translation) that belongs to the space of shape functions. We proceed as in the evaluation of the interpolation sub-pixel error (Section 6.2.5). From the displacement field evaluated on an image pair made of the reference picture and its translated copy, the standard deviation of the displacement field gives an *a priori* estimate of the measurement uncertainty. This uncertainty is usually much higher than the systematic error. It is customary to observe a dependence of the standard displacement uncertainty, σ_u, with the size, ℓ in pixels of the interrogation window (local approach) or elements (global approach using finite elements) as a power law

$$\sigma_u = A\ell^{-\eta} \tag{6.8}$$

where A is of the order of unity, and η varies between 1 and 2 as appropriate. This allows measurement uncertainties to be evaluated (excluding other factors related to noise or complexity of the observed displacement field) that commonly reach the hundredth or the even thousandth of one pixel in the most favorable cases.

From this estimate it is also possible to evaluate the strain uncertainty when they are obtained, say, by simple finite differences from the displacement field. It should be noted however that the fluctuations will be observed on strains are strongly correlated (or anti-correlated) at small scales. This is especially important for the subsequent use of those kinematic measurements for the identification of mechanical properties (see second part of this book) when these correlations are not taken into account. It is therefore advised to prefer formulations of inverse problems that are based on displacements rather than strains, or to be aware of the implicit filtering often linked to the strain calculation (see Chapter 7).

6.3.3. *Noise Sensitivity*

Another limiting factor is due to the presence of noise in images. This noise can be of different nature and therefore has very different statistical features. It can sometimes be reduced by image averaging, provided that the sample does not evolve (i.e.,

move) between acquisitions. A good approximation is often given by white noise (i.e., uncorrelated from pixel to pixel). Its effect can be followed up to the estimate of the displacement fluctuations. In the case of a local approach, when the correlation windows are not overlapping, then the displacement fluctuations exhibit no correlation between different discrete estimates. However when these windows overlap, or in the case of a global approach, the correlation matrix of the kinematic degrees of freedom is no longer diagonal but its calculation is possible for a low noise level using a linearized operator for the final stage of the displacement estimation [HIL 12a].

In general, the standard displacement uncertainty (i.e., its standard deviation σ_u) is proportional to that of the noise images ϵ (by linearity). The amplitude will be inversely proportional to the mean gradient of the image, and will decrease as a power law with the number of pixels that are used to measure the considered motion. Thus, in d dimensions, for both local and global approaches

$$\sigma_u \propto \frac{\epsilon}{\ell^{d/2}\langle|\boldsymbol{\nabla} f|^2\rangle^{1/2}} \tag{6.9}$$

A more detailed discussion of this evaluation is provided in References [BES 06, ROU 06, HIL 12a].

It is possible to take this expression as a practical recommendation on image quality and correlation parameters to use. Regarding the acquisition, it should minimize image noise (i.e., ϵ), and to acquire images with a large depth of gray level (as long as it is not effectively truncated by the noise level ϵ). The texture of the analyzed images also affects the displacement uncertainty. The dependence on the gray level gradient calls for textures having a high contrast, and secondly having a short correlation length. The limit to this suggestion is the ability to interpolate gray levels at a sub-pixel level, which instead requires a regular variation at the pixel level. A good compromise is to deal with textures whose correlation length (radius) is of the order of 2 to 5 pixels. Last, for the parameters of DIC itself, the size of correlation windows should increase to reduce its sensitivity to noise, but at the cost of lower spatial resolution. Again, a compromise must be made. One can also note that the sensitivity of different correlation algorithms vis-à-vis this image noise is not identical [DUP 10].

6.4. Stereo-Correlation or 3D-DIC

The main advantage of 2D DIC techniques described in Section 6.2 is their (apparent) simplicity and versatility, namely, a single camera is sufficient and the object surface preparation (when required) can be easily done (spraying paint is an easy way to create an appropriate speckle pattern at the surface of the object). However, some important points need to be kept in mind:

– by using a single camera only in-plane displacements/strains can be measured on a planar object,

– from a practical point of view the camera and the object need to be aligned so that the camera image plane and the planar object be parallel and remain parallel all along the experiment,

– if the object undergoes some out-of-plane displacements they will not be properly detected and they will produce in the images false apparent strains [SUT 08b].

With the stereo-correlation technique (also called 3D-DIC) that is described hereafter all these problems can be tackled. This technique allows to measure 3D displacements (in-plane and out-of-plane) and 2D strains undergone by any 3D object (not necessarily planar) while the experimental constraints are minimized [ORT 09a].

It should be noted that stereo-correlation procedures combine two techniques:

– *the DIC technique*, which is an image matching technique that allows to compute 2D displacement of pixels between two images. With this technique, several images taken at different instants with a single camera can be registered (see Section 6.2), or two images (or more) taken at the same instant by two cameras (or more) can be matched (see below).

– *the stereovision technique*, which is a triangulation-based 3D reconstruction technique, that allows to compute the 3D position of a scene point from its stereo projections in two images (or more).

6.4.1. *The stereovision technique*

Binocular stereovision is a technique for recovering the three-dimensional structure of a scene from two (or more) different viewpoints (Figure 6.6a where P is the 3-D point to be measured, p_1 and p_2 are its stereoprojections in the images, C_1 and C_2 are the optical centers of the two cameras).

From Figure 6.6a, we can see that it is possible to compute the 3D coordinates of point P provided that:

a) the two image-points p_1 and p_2, which correspond to the projection onto the images of the same physical point P, can be identified. This step is called *stereo image matching* or *search for stereo-correspondents*. It is the critical step of the stereovision technique (see Section 6.4.1.3).

b) the two lines $C_1\,p_1$ and $C_2\,p_2$ that intersect at P can be computed. This step requires that the intrinsic parameters (focal length, size of the pixels, distortion coefficients) of each camera and the extrinsic parameters of the stereo rig (relative position and orientation of the two cameras) be known. The intrinsic and extrinsic parameters are obtained by using an off-line calibration step (see Section 6.4.1.2).

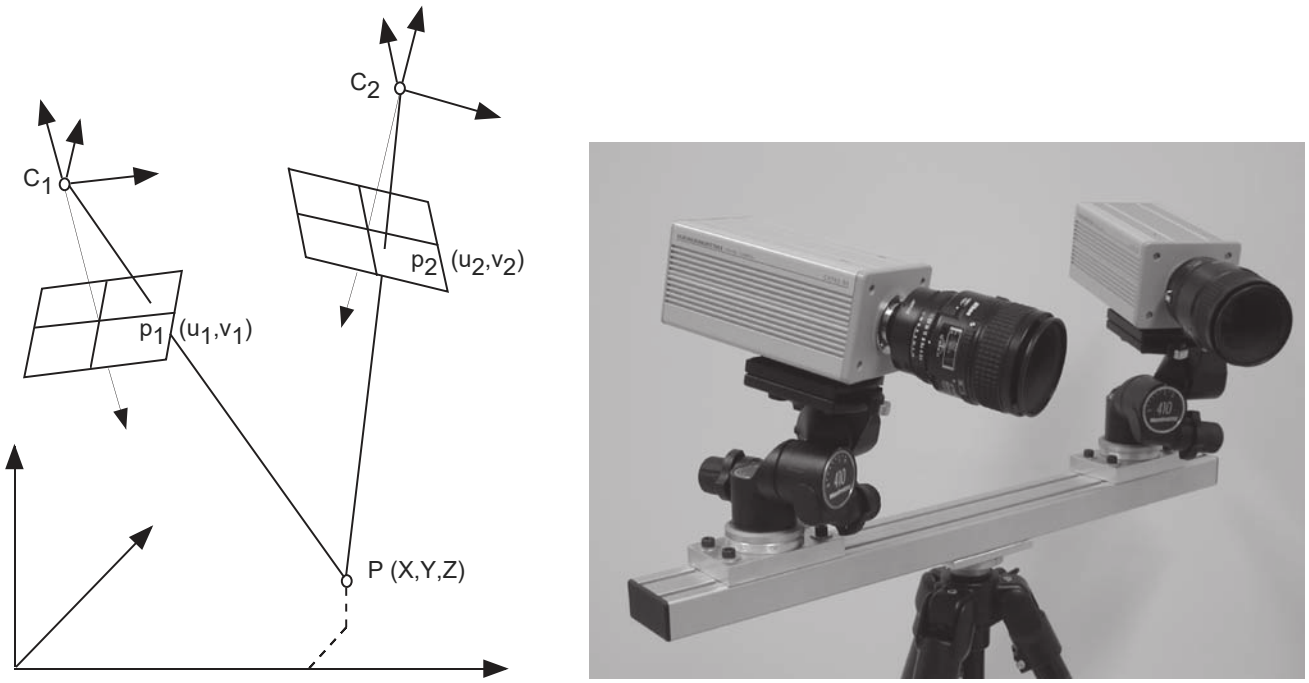

Figure 6.6. *(a) The principle of stereovision. (b) Picture of a stereo rig*

6.4.1.1. *Geometry of a stereovision sensor*

A binocular stereovision sensor is made up of two cameras positioned in such a way that their field of view intersects. Let us write $\mathcal{R}_c$ the reference frame associated to the left camera, $\mathcal{R}'_c$ the reference frame associated to the right camera, and $\mathcal{R}_w$ the so-called world reference frame in which the 3D measurements will be expressed. $\mathbf{T}$, $\mathbf{T}'$ and $\mathbf{T}_s$ are the rigid-body transformations (a rotation matrix and a translation vector) that link these reference frames (Figure 6.7). These three transformations are linked by: $\mathbf{T}_s = \mathbf{T}' \mathbf{T}^{-1}$. $\mathbf{T}_s$ is often called the *stereoscopic transformation*. It represents the orientation and translation of a camera with respect to the other one.

It should be noted that the 3D measurements are often expressed in the reference frame associated to the left or the right camera. In that case $\mathbf{T}$ or $\mathbf{T}'$ are the identity matrix.

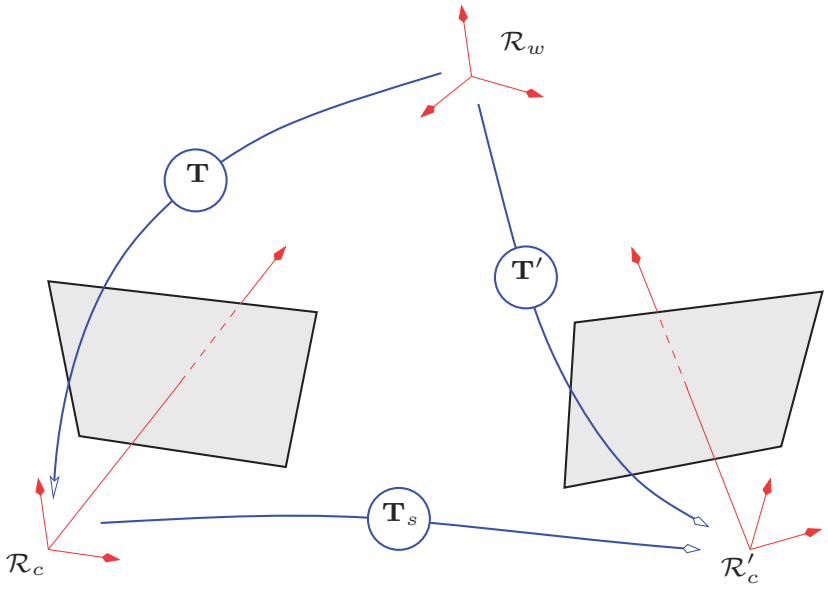

Figure 6.7. *The three reference frames associated to a stereovision sensor*

By modeling each camera by the classical linear *pinhole model* [6] and by writing $\mathbf{K}$ and $\mathbf{K}'$ the intrinsic parameters of the left and right camera respectively, the positions m and m' of the 2D image points corresponding to a 3D point M are written as [7]

$$\tilde{\mathsf{m}} = \mathbf{K}\,\mathbf{T}\,\tilde{\mathsf{M}} \tag{6.10}$$

$$\tilde{\mathsf{m}}' = \mathbf{K}'\,\mathbf{T}'\,\tilde{\mathsf{M}} = \mathbf{K}'\,\mathbf{T}_s\,\mathbf{T}\,\tilde{\mathsf{M}} \tag{6.11}$$

The image registration problem mentioned in Section 6.4.1 consists in finding the image-points m and m' that are stereo-correspondent.

In stereovision, the *epipolar geometry* [HOR 95] illustrated in Figure 6.8 provides the following important geometrical property (also called *epipolar constraint*):

> Given a point m in the left image, its corresponding point m' in the right image appears to be always lying along a line of the right image entirely defined by the coordinates of m. This line is called the *epipolar line* associated with m.

6. The pinhole model is based on the perspective projection. In such a model the distortions (which can be more or less important) induced by the lenses are not taken into account. For metrology applications, which require a high measurement accuracy, distortions need to be taken into account and more sophisticated camera models need to be used [GAR 01a, GAR 01b, COR 05b, ORT 09b, ORT 09a, SUT 09].

7. To be able to write the pinhole model in a matrix form, *homogeneous coordinates* are used [FAU 93, FAU 01]. $\tilde{\mathsf{m}}$ are the homogeneous coordinates associated to m.

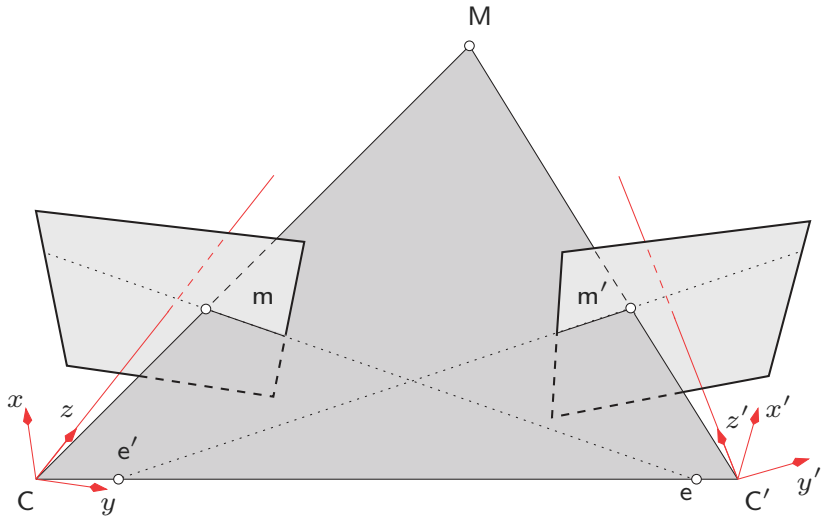

Figure 6.8. *The epipolar geometry: the epipolar lines are defined by the intersection of the image plane of each camera with the plane defined by points* M, C *and* C′, *where* C *and* C′ *are the optical centers of the left and right camera respectively*

Thanks to this important geometrical property, inherent to any stereo imaging system, the search for the stereo-correspondent of a given point in the left image is simplified from a 2D search across the entire image to a 1D search along its epipolar line. Using this geometrical constraint the image registration can be quicker and more robust (since possible false registration that could be found away from the epipolar line are avoided).

6.4.1.2. *Calibration of a stereovision sensor*

Camera calibration is an important task in 3D computer vision, particularly when metric data are required for applications involving accurate dimensional measurements. Calibrating a camera involves determining its intrinsic parameters (matrix $\mathbf{K}$, and possibly distortion parameters). Calibrating a stereovision sensor made up of two cameras involves determining the intrinsic parameters of each camera and the relative position and orientation between the two cameras ($\mathbf{T}_s$ transformation). These calibration data are required to compute, by triangulation, the 3D coordinates of a point corresponding to matched pixels on the two images. For more details on the calibration of a stereovision sensor, see References [GAR 01a, GAR 01b, ORT 09b].

6.4.1.3. *Matching of stereo images by DIC*

This section is dedicated to the matching of stereo images by DIC (which leads to the so-called *stereo-correlation* technique). It should be noted that stereovision can be used without DIC-based matching. It is for instance the case when stereo images are matched using feature matching [ORT 02, ORT 09a].

DIC-based image matching simply consists in using the DIC technique described in Section 6.2 in order to find stereo-correspondents. The only significant difference is that stereo-correlation can use (it is not compulsory) the epipolar constraint in order that the search for correspondent pixels be restricted to the epipolar line (or to a pixel band around the epipolar line).

6.4.1.4. *3D reconstruction by triangulation*

If the image-points $\mathsf{m} = (u, v)$ and $\mathsf{m}' = (u', v')$ (provided by the registration) and matrices $\mathbf{K}$, $\mathbf{K}'$, $\mathbf{T}$ and $\mathbf{T}_s$ (provided by the calibration of the stereovision sensor) are known, Equations (6.10) and (6.11) lead to an over-determined system of four equations and three unknowns that are the three coordinates of the searched 3D point $\mathsf{M} = (X, Y, Z)$ [HAR 97]:

$$\begin{pmatrix} u \\ v \\ u' \\ v' \end{pmatrix} = \begin{pmatrix} \\ H_{4\times 3} \\ \\ \end{pmatrix} \begin{pmatrix} X \\ Y \\ Z \end{pmatrix} \tag{6.12}$$

Equation (6.12) can be written as $b = H\,\mathsf{M}$ and the 3D coordinates of point M are determined analytically using the pseudo-inverse method

$$\mathsf{M} = \left[(H^T\,H)^{-1}\,H^T\right]\,b$$

The triangulation problem can also be solved using non-linear optimization by minimizing the distance between the measured image-points $(u, v)_m$ and the image-points $(u, v)_p$ predicted by the camera model [SUT 09]

$$\chi^2 = \sum \left((u_m - u_p)^2 + (v_m - v_p)^2 + (u'_m - u'_p)^2 + (v'_m - v'_p)^2\right) \tag{6.13}$$

Note that Equation (6.12) implies a linear model of the camera (pinhole model). When lens distortions are taken into account, the camera model is no longer linear. To compute the 3D coordinates of point M using Equation (6.12), the image-points need to be corrected for their distortion beforehand. If the distortion is not corrected beforehand, then Equation (6.13) needs to be used.

6.4.2. *3D displacement measurement by stereo-correlation*

Using the stereovision technique, the shape variation of an object can be measured by analyzing a sequence of pair of stereo images. However, in experimental mechanics, we are generally interested in the surface strain field, which can be obtained by tracking the displacement of some points at the surface of an object undergoing some mechanical or thermal loading as illustrated in Figure 6.9.

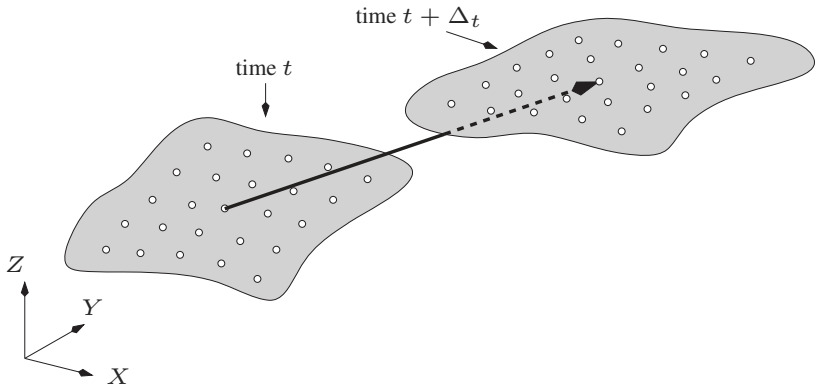

Figure 6.9. *3D displacement field corresponding to two deformation states of the object*

The 2D technique described in Section 6.2 allows the 2D displacement field to be computed at the surface of a planar object. By combining the stereo-correlation technique (DIC-based spatial registration between two cameras and triangulation, to get a cloud of 3D points) and the DIC-based temporal matching between the images acquired by the left or the right camera at different instants, the 3D displacement field of any object (with any complex shape) can be computed. This is illustrated in Figure 6.10.

This measurement technique provides the 3D displacements, from which the strains can be computed as described in the next section.

6.4.3. *Computation of surface strains from 3D displacements*

The stereo-correlation technique combined with temporal image matching leads to the 3D displacement field of any object with any complex shape (not necessarily planar). The surface strain field can be computed from the 3D displacement field by differentiation of the 3D displacement at each point of the surface, which can be a complex task.

From a practical point of view, the computation of the strain at a given point P of the surface is performed through several steps [COR 05a, SUT 09]:

– first, a small contiguous collection of 3D surface points (e.g., a 7×7 array with center-point P) is selected from the initial surface shape,

– next, a least squares plane is fitted to this 3D position data set providing the tangent plane,

– a local coordinate system $(\mathbf{n}, \mathbf{b}, \mathbf{t})$ is associated with the tangent plane and centered in P,

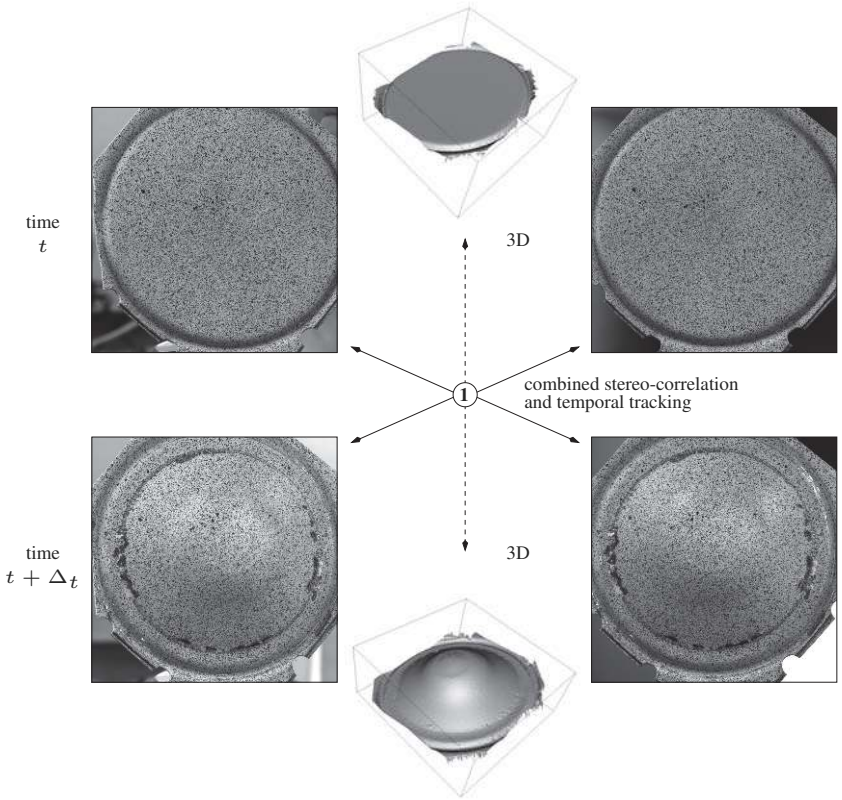

Figure 6.10. *3-D displacement field computation. Stereo-correlation (DIC-based spatial matching + triangulation) provides the shape of the object at a given instant. DIC-based temporal matching between the images taken by the left or right camera at different instants allows to temporally link the 3D points of the shapes*

– all displacement components for each point of the specimen points are converted into the local system. A set of displacement components (d_t, d_b, d_n) is obtained and written (d_X, d_Y, d_Z),

– the array of data points for each component of displacement is then fitted with a least squares functions of the form $\mathbf{g}(X, Y)$,

– differentiating the functional fit $\mathbf{g}(X, Y)$ for each displacement component in both the X and Y directions leads to the $\varepsilon_{XX}(\mathsf{P})$, $\varepsilon_{YY}(\mathsf{P})$ and $\varepsilon_{XY}(\mathsf{P})$ components of the strain tensor at point P.

6.4.4. *Applications*

The stereo-correlation technique has proven to be a powerful non-contact technique for measuring 3D displacement / 2D strain fields on any 3D object surface and is

now widely used for industrial applications in different fields of mechanics and materials [SUT 09], namely, fracture mechanics [SUT 92, LUO 94, LUO 00, SUT 07b], biomechanics [SUT 08a, TYS 02], for the study of different types of materials, namely, composites [MCG 01, LOP 04, MUL 05, KAR 06], ceramics / concrete [ORT 07, ROB 07], foams [GUA 07], elastomers [MIS 05, JON 06], tyre [MOS 07], soft membranes [VIA 05]. The technique is very versatile and can be used for a large scale of experimental mechanics problems. It was applied at micro [SCH 04] or macro scales [HEL 03] (small or large structures), it can measure both small (a few hundreds of micro-strains) and large strains ($>$200%), it can be used for high-speed dynamic tests by using high-speed cameras [SCH 03a, SCH 03b, SIE 07, TIW 07, BES 08, BES 10].

6.5. Conclusions

Digital image correlation, as we have seen through its many variants, in two or three dimensions, surface and even volume, at different scales of space and time allows for the measurement of displacement fields with a rich description and remarkable accuracy especially in light of its ease of implementation. Image correlation can exploit with great flexibility pictures acquired by different imaging means every day better and more informative. Many tools are available to incorporate in this measurement procedure any a priori knowledge that is available on the kinematics to assess the measurement uncertainty, or the covariance matrix of the measured degrees of freedom induced by image noise, and finally to visualize the residual field, often carrying very valuable information. Today's experiments provide a number of measured data comparable or sometimes even higher than what traditionally was the privilege of numerical simulations.

These measurements are used, and currently more often than never before, to monitor mechanical tests, whether in the context of conventional characterization, or when used in an industrial context. The latter distinction is increasingly blurred as kinematic measurements, in particular by stereo-correlation, can account for complex loadings and geometries. This merger opens up outstanding perspectives in terms of quantitative use of tests, and therefore relevant responses to the use of materials, structures, or assemblies under realistic conditions, representative of their in-service life.

Last, what explains the spectacular development of this technique is probably its coupling with numerical simulations for identification and validation purposes. The end of the book is devoted to this broad issue. Again the classical boundary between experimental and numerical fields gradually vanishes, thanks to measured fields. They thus appear in different dimensions as the focal point to a particularly fruitful dialogue between all actors interested in the mechanical behavior of materials and structures, experimentalists and modelers, designers and users, researchers and producers.

6.6. Bibliography

[ALL 94] ALLAIS L., BORNERT M., BRETHEAU T., CALDEMAISON D., "Experimental characterization of the local strain field in a heterogeneous elastoplastic material", *Acta Mater.*, vol. 42, num. 11, p. 3865–3880, 1994.

[BAY 99] BAY B. K., SMITH T. S., FYHRIE D. P., SAAD M., "Digital volume correlation: three-dimensional strain mapping using X-ray tomography", *Exp. Mech.*, vol. 39, p. 217–226, 1999.

[BAY 08] BAY, B. K., "Methods and applications of digital volume correlation", *J. Strain Anal. Eng. Design*, vol. 43, num. 8, p. 745-760, 2008.

[BEN 09] BENOIT A., GUÉRARD S., GILLET B., GUILLOT G., HILD F., MITTON D., PÉRIÉ J.-N., ROUX S., "3D analysis from micro-MRI during *in situ* compression on cancellous bone", *J. Biomechanics*, vol. 42, p. 2381–2386, 2009.

[BES 06] BESNARD G., HILD F., ROUX S., "Finite-element displacement fields analysis from digital images: Application to Portevin-Le Chatelier bands", *Exp. Mech.*, vol. 46, p. 789–803, 2006.

[BES 08] BESNARD G., ETCHESSAHAR B., LAGRANGE J.-M., VOLTZ C., HILD F., ROUX S., "Metrology and detonics: analysis of necking", *Proceedings 28th International Congress on High-Speed Imaging and Photonics, (SPIE)*, 71261N, 2008, (doi:10.1117/12.821892).

[BES 10] BESNARD G., LAGRANGE J.-M., HILD F., ROUX S., VOLTZ C., "Characterization of necking phenomena in high speed experiments by using a single camera", *EURASIP J. Im. Video. Proc.*, vol. 2010, num. 215956, 2010, 15 p.

[BOR 04] BORNERT M., CHAIX J.-M., DOUMALIN P., DUPRÉ J.-C., FOURNEL T., JEULIN D., MAIRE E., MOREAUD M., MOULINEC H., "Mesure tridimensionnelle de champs cinématiques par imagerie volumique pour l'analyse des matériaux et des structures", *Inst. Mes. Métrol.*, vol. 4, p. 43–88, 2004.

[BOR 09] BORNERT M., BRÉMAND F., DOUMALIN P., DUPRÉ J.-C., FAZZINI M., GRÉDIAC M., HILD F., MISTOU S., MOLIMARD J., ORTEU J.-J., ROBERT L., SURREL Y., VACHER P., WATTRISSE B., "Assessment of digital image correlation measurement errors: methodology and results", *Exp. Mech.*, vol. 49, p. 353–370, 2009.

[BUR 82] BURT P. J., YEN C., XU X., "Local correlation measures for motion analysis: a comparative study", *Proceedings IEEE Conf. on Pattern Recognition and Image Processing*, p. 269–274, 1982.

[CHA 11] CHAMBON S., CROUZIL A., "Similarity measures for image matching despite occlusions in stereo vision", *Pattern Recognition*, vol. 44, num. 9, p. 2063–2075, 2011.

[CHA 02] CHASIOTIS I., KNAUSS W.G., "A new microtensile tester for the study of MEMS materials with the aid of atomic force microscopy ", *Exp. Mech.*, vol. 42, p. 51–57, 2002.

[CH0 97] CHOI S., SHAH S.P., "Measurement of deformations on concrete subjected to compression using image correlation ", *Exp. Mech.*, vol. 37, p. 307–313, 1997.

[CHO 05b] CHO S. W., CHASIOTIS I., FRIEDMAN T. A., SULLIVAN J., "Young's modulus, Poisson's ratio and failure properties of tetrahedral amorphous diamond-like carbon for MEMS devices", *J. Micromech. Microeng.*, vol. 25, p. 728–735, 2005.

[CHO 07a] CHO S. W., CHASIOTIS I., "Elastic properties and representative volume element of polycrystalline silicon for MEMS", *Exp. Mech.*, vol. 47, p. 37–49, num. 1, 2007.

[CHO 07b] CHO S. W., JONNALAGADDA K., CHASIOTIS I., "Mode I and mixed mode fracture of polysilicon for MEMS", *Fatigue & Fract. Eng. Mat. Struct.*, vol. 30, p. 21–31, January 2007.

[COR 05a] CORNILLE N., Accurate 3D Shape and Displacement Measurement using a Scanning Electron Microscope, PhD thesis, INSA Toulouse (France) and University of South Carolina (Columbia, USA), 2005.

[COR 05b] CORNILLE N., GARCIA D., SUTTON M.A., MCNEILL S., ORTEU J.-J., "Calibrage d'imageurs avec prise en compte des distorsions", *Inst. Mes. Métrol.*, vol. 4, num. 3-4/2004, p. 105–124, 2005.

[DAU 11] DAUTRIAT J., BORNERT M., GLAND N., DIMANOV A., RAPHANEL J., "Localized deformation induced by heterogeneities in porous carbonate analysed by multi-scale digital image correlation", *Tectonophysics*, vol. 503, num. 1-2, p. 100–116, 2011.

[DOU 00a] DOUMALIN P., BORNERT M., "Micromechanical applications of digital image correlation techniques", *Interferometry in Speckle Light: Theory and Applications*, P. Jacquot and J.M. Fournier Eds., Springer p. 67–74, 2000.

[DOU 00b] DOUMALIN P., "Microextensométrie locale par corrélation d'images numériques ; Application aux études micromécaniques par microscopie électronique à balayage.", PhD thesis (in French), École polytechnique (France), 2000.

[DOU 03] DOUMALIN, P., BORNERT, M., CRÉPIN, J., "Caractérisation de la répartition de la déformation dans les matériaux hétérogènes ", *Méc. et Ind.* , vol. 4, p. 607–617, 2003.

[DUP 10] DUPRÉ J.C, BORNERT M., ROBERT L., WATTRISSE B., "Digital image correlation: displacement accuracy estimation", Proceedings of the 14th International Conference on Experimental Mechanics, 8 pages, 2010.

[FAU 93] FAUGERAS O., *Three-Dimensional Computer Vision: A Geometric Viewpoint*, The MIT Press, 1993.

[FAU 01] FAUGERAS O., LUONG Q. T., PAPADOPOULOS T., *The Geometry of Multiple Images*, The MIT Press, 2001.

[GAR 01a] GARCIA D., Mesure de formes et de champs de déplacements tridimensionnels par stéréo-corrélation d'images, PhD thesis (in French), Institut National Polytechnique de Toulouse (France), 2001.

[GAR 01b] GARCIA D., ORTEU J.-J., DEVY M., "Calibrage précis d'une caméra CCD ou d'un capteur de vision stéréoscopique", *Photomécanique 2001*, Futuroscope, Poitiers (France), p. 24–26, 2001.

[GUA 07] GUASTAVINO R., GÖORANSSON P., "A 3D displacement measurement methodology for anisotropic porous cellular foam materials", *Polymer Testing*, vol. 26, num. 6, p. 711–719, 2007.

[HAL 10] HALL S., BORNERT M., DESRUES J., PANNIER Y., LENOIR N., VIGGIANI C., BÉSUELLE P. , "Discrete and Continuum analysis of localised deformation in sand using X-ray micro CT and Volumetric Digital Image Correlation", *Geotech.*, vol. 60, num. 5, p. 315–322, 2010.

[HAN 10] HAN K., CICCOTTI M., ROUX S., "Measuring nanoscale stress intensity factors with an Atomic Force Microscope", *EuroPhys. Lett.*, vol. 89, p. 66003, 2010.

[HAR 97] HARTLEY R. I., STURM P., "Triangulation", *Computer Vision and Image Understanding (CVIU'97)*, vol. 68, num. 2, p. 146–157, 1997.

[HEL 03] HELM J. D., SUTTON M. A., MCNEILL S. R., "Deformations in wide, center-notched, thin panels, part I: three-dimensional shape and deformation measurements by computer vision", *Opt. Eng.*, vol. 42, num. 5, p. 1293–1305, 2003.

[HER 07] HERIPRE E., DEXET M., CREPIN J., GELEBART L., ROOS A., BORNERT M., CALDEMAISON D., "Coupling between experimental measurements and polycrystal finite element calculations for micromechanical study of metallic materials", *Int. J. Plast.*, vol. 23, num. 9, p. 1512-1539, 2007.

[HIL 02] HILD F., RAKA B., BAUDEQUIN M., ROUX S., CANTELAUBE F., "Multiscale displacement field measurements of compressed mineral-wool samples by digital image correlation", *Appl. Opt.*, vol. 41, num. 32, p. 6815–6828, 2002.

[HIL 06] HILD F., ROUX S., "Digital image correlation: from displacement measurement to identification of elastic properties – A review", *Strain*, vol. 42, p. 69–80, 2006.

[HIL 09a] HILD F., ROUX S., GRAS R., MARANTE M. E., GUERRERO N., FLÓREZ-LÓPEZ J., "Displacement Measurement Technique for Beam Kinematics", *Opt. Lasers Eng.*, vol. 47, p. 495–503, 2009.

[HIL 09b] HILD F., MAIRE E., ROUX S., WITZ J.-F., "Three dimensional analysis of a compression test on stone wool", *Acta Mat.*, vol. 57, p. 3310–3320, 2009.

[HIL 12a] HILD F., ROUX S., "Comparison of local and global approaches to digital image correlation", *Exp. Mech.*, DOI 10.1007/s11340-012-9603-7, 2012.

[HIL 12b] HILD F., ROUX S., "Digital Image Correlation", RASTOGI, P., HACK, E., Eds., *Optical Methods for Solid Mechanics. A practical guide*, Wiley, 2012, in press.

[HOR 95] HORAUD R., MONGA O., *Vision par ordinateur : outils fondamentaux*, Hermès, 1995, deuxième édition.

[JON 06] JONES A., SHAW J., WINEMAN A., "An Experimental Facility to Measure the Chemorheological Response of Inflated Elastomer Membranes at High Temperature", *Exp. Mech.*, vol. 46, num. 5, p. 579–587, 2006.

[KAR 06] KARAMA M., LORRAIN B., "Modélisation numérique et expérimentale du comportement de structures sandwich", *Mécanique & Industries*, vol. 7, p. 39–48, 2006.

[LEC 09] LECLERC H., PÉRIÉ J.-N., ROUX S., HILD F., "Integrated Digital Image Correlation for the Identification of Material Properties", *Lecture notes in computer science*, vol. 5496, p. 161–171, 2009.

[LEC 11] LECLERC H., PÉRIÉ J.-N., ROUX S., HILD F., "Voxel-scale digital volume correlation", *Exp. Mech.*, vol. 51, num. 4, 2011, p. 479–490.

[LEN 07] LENOIR N, BORNERT M., DESRUES J., BESUELLE P., VIGGIANI, G., "Volumetric digital image correlation applied to X-ray microtomography images from triaxial compression tests on argillaceous rock", *Strain*, vol. 43, num. 3, p. 193–205, 2007.

[LEP 07] LEPRINCE S., BARBOT S., AYOUB F., AVOUAC J.-P., "Automatic and precise orthorectification, coregistration, and subpixel correlation of satellite images, application to ground deformation measurements ", *IEEE T. Geosci. Remote*, vol. 45, num. 6, Part 1, p. 1529-1558, 2007.

[LOP 04] LOPEZ-ANIDO R., EL-CHITI F. W., MUSZYÑSKI L., DAGHER H. J., THOMPSON L. D., HESS P. E., "Composite Material Testing using a 3-D Digital Image Correlation System", *Proc. of Composites 2004 Conference*, Tampa (Florida, USA), 2004.

[LUC 81] LUCAS B. D., KANADE T., "An iterative image registration technique with an application to stereo vision", *Proceedings of the 7th international joint conference on Artificial intelligence, IJCAI'81*, vol. 2, p. 674–679, (Morgan Kaufmann Publishers Inc., San Francisco, CA, USA), 1981.

[LUO 94] LUO P. F., CHAO Y. J., SUTTON M. A., "Application of stereo vision to three-dimensional deformation analyses in fracture experiments", *Opt. Eng.*, vol. 33, num. 3, p. 981–990, 1994.

[LUO 00] LUO P. F., HUANG F. C., "Application of stereovision to the study of mixed-mode crack-tip deformations", *Opt. Lasers Eng.*, vol. 33, num. 5, p. 349–368, 2000.

[MCG 01] MCGOWAN D. M., AMBUR D. R., HANNA T. G., MCNEILL S. R., "Evaluating the Compressive Response of Notched Composite Panels Using Full-Field Displacements", *Journal of Aircraft*, vol. 38, num. 1, p. 122–129, American Institute of Aeronautics and Astronautics (AIAA), 2001.

[MIS 05] MISTOU S., KARAMA M., DESMARS B., PERES P., PIRON E., HEUILLET P., "Application de la méthode de stéréocorrélation d'images à la caractérisation des élastomères en grandes déformations", *Inst. Mes. Métrol.*, vol. 4, num. (3-4) p. 147–166, 2005.

[MOS 07] MOSER R., LIGHTNER III J. G., "Using Three-Dimensional Digital Imaging Correlation Techniques to Validate Tire Finite-Element Model", *Exp. Tech.*, vol. 31, num. 4, p. 29–36, 2007.

[MUL 05] MULLE M., PÉRIÉ J.-N., ROBERT L., COLLOMBET F., GRUNEVALD Y., "Mesures de champs par stéréo-corrélation sur structures composites instrumentées par fibres optiques à réseaux de Bragg", *Inst. Mes. Métrol.*, vol. 4, num. (3-4) p. 167–192, 2005.

[NEU 08] NEU C. P., WALTON J. H., "Displacement encoding for the measurement of cartilage deformation", *Magn. Reson. Med.*, vol. 59, p. 149–155, 2008.

[ORT 02] ORTEU J.-J., "Mesure 3D de formes et de déformations par stéréovision", *Les Techniques de L'Ingénieur*, vol. BM 7015 of *Traité Génie Mécanique – Travail des matériaux*, 2002.

[ORT 07] ORTEU J.-J., CUTARD T., GARCIA D., CAILLEUX E., ROBERT L., "Application of Stereovision to the Mechanical Characterisation of Ceramic Refractories Reinforced with

Metallic Fibres", *Strain*, vol. 43, num. 2, p. 96–108, 2007.

[ORT 09b] ORTEU J.-J., "Calibrage géométrique d'une caméra ou d'un capteur de vision stéréoscopique", Ressources en ligne UNIT "Optique pour l'Instrumentation", 2009, `http://optique-instrumentation.fr/`.

[ORT 09a] ORTEU J.-J., "3-D Computer Vision in Experimental Mechanics", *Opt. Lasers Eng.*, vol. 47, num. 3-4, p. 282–291, 2009.

[POL 02] POLLEFEYS M., "Visual 3D Modeling from Images - A Tutorial", Available online: `http://www.cs.unc.edu/~marc/tutorial/`, 2002.

[RAN 10] RANNOU J., LIMODIN N., RÉTHORÉ J., GRAVOUIL A., LUDWIG W., BAÏETTO-DUBOURG M.-C., BUFFIÈRE J.-Y., COMBESCURE A., HILD F., ROUX S., "Three dimensional experimental and numerical multiscale analysis of a fatigue crack", *Comp. Meth. Appl. Mech. Eng.*, vol. 199, p. 1307–1325, 2010.

[RET 08] RÉTHORÉ J., HILD F., ROUX S., "Extended digital image correlation with crack shape optimization", *Int. J. Num. Meth. Eng.*, vol. 73, p. 248–272, 2008.

[RET 09a] RÉTHORÉ J., ELGUEDJ T., SIMON P., CORET M., "On the use of NURBS functions for displacement derivatives measurement by digital image correlation", *Exp. Mech.*, vol. 50, num. 7, 2009, p. 1099–1116.

[RET 09b] RÉTHORÉ J., HILD F., ROUX S., "An extended and integrated digital image correlation technique applied to the analysis fractured samples", *Eur. J. Comput. Mech.*, vol. 18, p. 285–306, 2009.

[ROB 07] ROBERT L., NAZARET F., CUTARD T., ORTEU J.-J., "Use of 3-D Digital Image Correlation to Characterize the Mechanical Behavior of a Fiber Reinforced Refractory Castable", *Exp. Mech.*, vol. 47, num. 6, p. 761–773, December 2007.

[ROU 05] ROUX S., HILD F., PAGANO S., "A stress scale in full-field identification procedures: A diffuse stress gauge", *Eur. J. Mech. A/Solids*, vol. 24, p. 442–451, 2005.

[ROU 06] ROUX S., HILD F., "Stress intensity factor measurements from digital image correlation: Post-processing and integrated approaches", *Int. J. Fract.*, vol. 140, p. 141–157, 2006.

[ROU 08] ROUX S., HILD F., VIOT P., BERNARD, D., "Three dimensional image correlation from X-Ray computed tomography of solid foam", *Comp. Part A*, vol. 39, p. 1253–1265, 2008.

[ROU 09] ROUX S., RÉTHORÉ J., HILD F., "Digital Image Correlation and Fracture: An Advanced Technique for Estimating Stress Intensity Factors of 2D and 3D Cracks", *J. Phys. D: Appl. Phys.* vol. 42, p. 214004, 2009.

[ROU 12] ROUX S., HILD F., LECLERC H., "Mechanical assistance to DIC", *Proceedings Full field measurements and identification in Solid Mechanics*, Cachan, 2012, Elsevier, IUTAM Procedia, in press.

[RUP 07] RUPIN N., "Déformation à chaud de métaux biphasés : modélisations théoriques et confrontations expérimentales", PhD thesis (in French), École polytechnique (France), 2007.

[SCA 92] SCAMBOS T.A., DUTKIEWICZ M.J., WILSON J.C., BINDSCHADLER, R.A., "Application of image cross-correlation to the measurement of glacier velocity using satellite image data ", *Remote Sens. Environ.*, vol. 42, num. 3, p. 177-186, 1992.

[SCH 03a] SCHMIDT T. E., TYSON J., GALANULIS K., "Full-Field Dynamic Displacement and Strain Measurement – Specific Examples Using Advanced 3D Image Correlation Photogrammetry: Part II", *Exp. Tech.*, vol. 27, num. 4, p. 22–26, 2003.

[SCH 03b] SCHMIDT T. E., TYSON J., GALANULIS K., "Full-Field Dynamic Displacement and Strain Measurement Using Advanced 3D Image Correlation Photogrammetry: Part I", *Exp. Tech.*, vol. 27, num. 3, p. 47–50, 2003.

[SCH 00] SCHREIER H. W., BRAASCH J. R., SUTTON M. A., "Systematic errors in digital image correlation caused by intensity interpolation", *Opt. Eng.*, vol. 39, num. 11, p. 2915–2921, 2000.

[SCH 04] SCHREIER H. W., GARCIA D., SUTTON M. A., "Advances in light microscope stereo vision", *Exp. Mech.*, vol. 44, num. 3, p. 278–288, 2004.

[SCR 07] SCRIVENS W. A., LUO Y., SUTTON M. A., COLLETTE S. A., MYRICK M. L., MINEY P., COLAVITA P. E., REYNOLDS A. P., LI X., "Development of Patterns for Digital Image Correlation Measurements at Reduced Length Scales", *Exp. Mech.*, vol. 47, num. 1, p. 63–77, 2007.

[SIE 07] SIEBERT T., BECKER T., SPILTTHOF K., NEUMANN I., KRUPKA R., "High-speed digital image correlation: error estimations and applications", *Opt. Eng.*, vol. 46, num. 5, Page051004, 2007.

[SOP 01] SOPPA E., DOUMALIN P., BINKELE P., WIESENDANGER T., BORNERT M., SCHMAUDER S., "Experimental and numerical characterisation of in-plane deformation in two-phase materials", *Comput. Mat. Sci.*, vol. 21, num. 3, p. 261–275, 2001.

[SUT 83] SUTTON M. A., WOLTERS W. J., PETERS W. H., RANSON W. F., MCNEILL S. R., "Determination of Displacements Using an Improved Digital Correlation Method ", *Im. Vis. Comp.*, vol. 1, num. 3, p. 133–139, 1983.

[SUT 86] SUTTON M. A., CHENG M., PETERS W. H., CHAO Y. J., MCNEILL S. R., "Application of an optimized digital correlation method to planar deformation analysis ", *Im. Vis. Comp.*, vol. 4, num. 3, p. 143–150, 1986.

[SUT 92] SUTTON M. A., TURNER J. L., CHAO Y. J., BRUCK H. A., CHAE T. L., "Experimental investigations of three-dimensional effects near a crack tip using computer vision", *Int. J. Fract.*, vol. 53, num. 3, p. 201–228, 1992.

[SUT 06] SUTTON, M.A., LI, N., GARCIA, D., CORNILLE, N., ORTEU, J.-J., MCNEILL, S.R., SCHREIER, H.W., LI, X., "Metrology in a scanning electron microscope: theoretical developments and experimental validation", *Meas. Sci. Technol.*, vol. 17, num. 10, p. 2613–2622, 2006.

[SUT 07a] SUTTON M. A. , LI N., JOY D. C., REYNOLDS A. P., LI X., "Scanning Electron Microscopy for Quantitative Small and Large Deformation Measurements Part I: SEM Imaging at Magnifications from 200 to 10,000", *Exp. Mech.*, vol. 47, num. 6, p. 775–787, 2007.

[SUT 07b] SUTTON M. A., YAN J., DENG X., CHENG C.-S., ZAVATTIERI P., "Three-dimensional digital image correlation to quantify deformation and crack-opening displacement in ductile aluminum under mixed-mode I/III loading", *Opt. Eng.*, vol. 46, num. 5, Page 051003, 2007.

[SUT 08a] SUTTON M. A., KE X., LESSNER S. M., GOLDBACH M., YOST M., ZHAO F., SCHREIER H. W., "Strain Field Measurements on Mouse Carotid Arteries using Microscopic Three Dimensional Digital Image Correlation", *J. Biomedical Mat. Res. Part A*, vol. 84, num. 1, p. 178–190, 2008.

[SUT 08b] SUTTON M. A., YAN J. H., TIWARI V., SCHREIER H. W., ORTEU J.-J., "The Effect of Out of Plane Motion on 2D and 3D Digital Image Correlation Measurements", *Opt. Lasers Eng.*, vol. 46, num. 10, p. 746–757, 2008.

[SUT 09] SUTTON M. A., ORTEU J.-J., SCHREIER H. W., *Image Correlation for Shape, Motion and Deformation Measurements – Basic Concepts, Theory and Applications*, Springer-Verlag New York Inc., 2009.

[TAT 05] TATSCHL A., KOLEDNIK O., "On the experimental characterization of crystal plasticity in polycrystals", *Mat. Sci. Eng. A-Struct.*, vol. 342, num. 1–2, p. 152–168, 2003.

[TER 09] TERZI S., SALVO L., SUERY M., LIMODIN N., ADRIEN J., MAIRE E., PANNIER Y., BORNERT M., BERNARD D., FELBERBAUM M., RAPPAZ M., BOLLER E., "In situ X-ray tomography observation of inhomogeneous deformation in semi-solid aluminium alloys", *Scripta Mater.*, vol. 61, num. 5, p. 449–452, 2009.

[TIW 07] TIWARI V., SUTTON M. A., MCNEILL S. R., "Assessment of High Speed Imaging Systems for 2D and 3D Deformation Measurements: Methodology Development and Validation", *Exp. Mech.*, vol. 47, num. 4, p. 561–579, 2007.

[TYS 02] TYSON J., SCHMIDT T., GALANULIS K., "Biomechanics Deformation and Strain Measurements With 3D Image Correlation Photogrammetry", *Exp. Tech.*, vol. 26, num. 5, p. 39–42, 2002.

[VIA 05] VIALETTES P., SIGUIER J.-M., GUIGUE P., MISTOU S., DALVERNY O., KARAMA M., PETITJEAN F., "Etude par stéréo-corrélation de sous-ensembles de ballons stratosphériques pressurisés", *Inst. Mes. Métrol.*, vol. 4, num. (3-4) p. 125–145, 2005.

[WAN 09] WANG, Y. Q., SUTTON, M. A., BRUCK, H. A., SCHREIER, H. W., "Quantitative Error Assessment in Pattern Matching: Effects of Intensity Pattern Noise, Interpolation, Strain and Image Contrast on Motion Measurements", *Strain*, vol. 45, num. 2, p. 160–178, 2009.

[WAT 01] WATTRISSE B., CHRYSOCHOOS A., MURACCIOLE J.-M., NÉMOZ-GAILLARD M. N., "Analysis of Strain Localization during Tensile Tests by Digital Image Correlation", *Exp. Mech.*, vol. 41, p. 29–39, 2001.

[WIL 57] WILLIAMS M. L., "On the stress distribution at the base of a stationary crack", *ASME J. Appl. Mech.*, vol. 24, p. 109–114, 1957.

[YAN 10] YANG D.S., BORNERT M., GHARBI H., VALLI P., WANG L.L., "Optimized optical setup for DIC in rock mechanics", Proceedings of the 14th International Conference on Experimental Mechanics, 8 pages, 2010.